Simulation of Photoacoustic Wave Generation and Propagation in Fluid-Solid Coupled Media Using Finite Integration Technique

Kazuyuki Nakahata$^{(\boxtimes)}$ (iD), Akihiro Miki, and Taizo Maruyama

Ehime University, Bunkyo 3, Matsuyama, Ehime 790-8577, Japan
nakahata@cee.ehime-u.ac.jp

Abstract. Photoacoustic (PA) waves using the transmission of a laser beam are being introduced in recent nondestructive ultrasonic testing. Not parameters related to acoustic, optic, and thermal phenomena but also spatial and time conditions of the laser irradiation affect the generation of the PA wave. Therefore, an appropriate design and preparation are required for reliable laser ultrasonic testing. Numerical simulation can be an effective tool for predicting PA signals. This study aims to develop a numerical model to simulate PA wave generation and propagation. Here, the heat conduction and the elastic wave equations were solved in a coupled manner based on discretization by the finite integration technique (FIT). We simulated two cases where the laser were irradiated on the target material in the air and underwater. The amplitude of the longitudinal PA wave propagating in the depth direction in the case of laser irradiation in water became more extensive than in the case of laser irradiation in the air. This reason was that the presence of water in the upper part caused a reaction force against the stress generated by thermal expansion. The FIT simulation was validated by experimental measurement of the PA wave.

Keywords: Laser ultrasonics · Photoacoustic wave · Coupled finite integration technique · Simulation · Experimental measurement · Solid-water interface

1 Introduction

Laser ultrasonics in nondestructive testing (NDT) is a technology for transmitting and receiving ultrasonic waves in a non-contact manner. Since laser ultrasonics enables us to generate ultrasonic waves at a distance from the target object, it is effective for inspection of structural components in infrastructure [1, 2]. Laser ultrasonics uses different mechanisms for transmitting and receiving ultrasonic waves [3]. For the transmission, a pulse laser beam is irradiated onto the surface of the target to generate an ultrasonic wave into the target. On the other hand, a continuous laser pulse is irradiated onto the target surface to receive ultrasound waves. At that time, surface deformation is detected using interference between reflected and reference light. A combination of ultrasonic transmission and reception makes a complete non-contact inspection [4, 5] possible.

There are two ways to generate the ultrasonic wave using the laser as shown in Fig. 1. One is a laser ablation that needs intense pulse energy (Fig. 1(a)). Although the laser ablation mode might deface the target material, several NDT case studies using the ablation mode [6] and the modeling [7] have been reported. The other is a photoacoustic (PA) mode, sometimes called a thermal expansion mode, that uses small laser energy compared with laser ablation (Fig. 1(b)). In the PA mode, the sudden change and confinement of heat generate the stress wave with an ultrasonic frequency range. Diagnostic imaging methods [8] using the PA wave are being introduced actively in the medical field. A photoacoustic microscopy (PAM) using the PA wave was developed as a tool for visualizing vascular networks [9], and recent applications propose a measurement of the oxygen saturation in the vascular [10] based on the difference of light absorption by wavelength. In the human body, the laser penetrates the interior of the body so that PA waves are generated from internal light absorbers such as blood, lipids, lymph, and among others [11]. However, the laser cannot penetrate a deeper portion of industrial materials such as metal and concrete, and the PA wave generates near the surface. Therefore, the generating position of the PA wave and its spreading characteristics in the NDT application are different from those in the medical one.
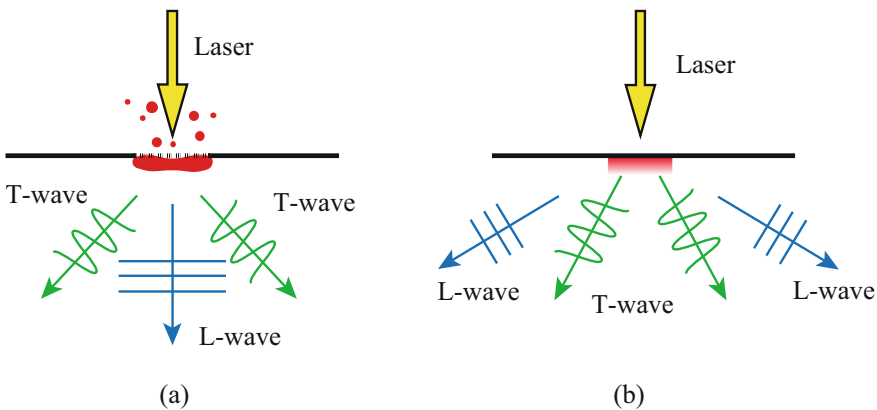

Fig. 1. Ultrasonic wave generation by (a) laser ablation and (b) photoacoustic phenomenon

Theoretical and experimental investigations for the laser ultrasonics for the NDT were carried out widely and diligently in the 1980s [12]. Since entering the 21st century, numerical models for laser ultrasonics have been proposed due to advances in hardware performance and computational techniques. To model the generation and propagation of PA waves induced by laser, it is necessary to solve the coupled equations of heat conduction and wave equation. Yoshikawa and Nishimura [13] analyzed the coupled problem of thermal expansion of a material due to laser irradiation and elastic wave generation in a semi-infinite three-dimensional domain using the boundary element method. Effects of a laser pulse duration and a beam radius in PA wave generation were investigated using the finite element method [14]. Although the laser pulse duration is on the order of nanoseconds, the propagation time of the PA wave in a solid is several tens of microseconds in general nondestructive testing. This time-scale difference sometimes

needs technical and computational operations to simulate the entire process from generating and propagating PA waves in the target area [15]. Nevertheless, the actual PA signal might be received with a low frequency due to the material attenuation and the bandwidth limitation of the receiving sensor. Therefore, a simplified model based on the directivity pattern [16] shown in Fig. 2 is often incorporated into the simulation without solving the coupled equation rigorously. Figure 2 shows the analytical representation of the radiation patterns of longitudinal (L) and transverse (T) waves generated in laser irradiation. This was derived assuming the surface is traction free, and light penetration is very small compared to the acoustic wavelength. In reality, however, the PA waves generated by pulsed laser irradiation highly depend on the laser intensity, pulse duration, spot size, physical properties of the material, interface conditions, etc. Therefore, it should be carefully confirmed whether the model in Fig. 2 is applicable in advance.

We here present a simulation method of the PA wave. In this study, we couple both the heat conduction equation and the wave equation in the framework of the finite integration technique [17] (FIT) to simulate the generation of thermal stresses and the propagation of the PA wave rigorously. Here we model the PA wave generation and propagation in solid using the coupled FIT approach. Sometimes, the laser is used in fluid as water, so it should be helpful to investigate the PA wave by considering the effect with or without a fluid layer. Further, a validation of the simulation is discussed using the PA wave measurement in the later section. Finally, we summarize our research findings and mentions future lines of work.
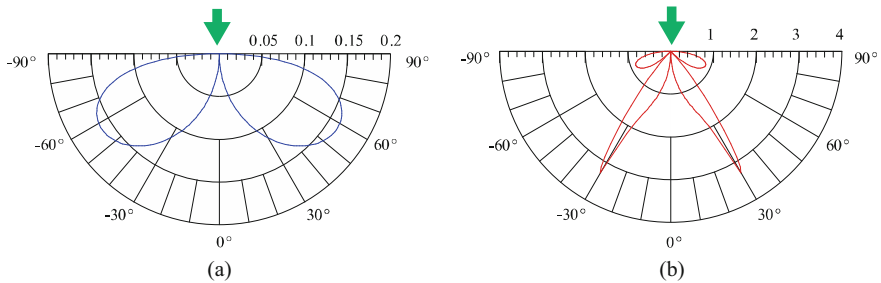

Fig. 2. (a) Directivities of (a) L-wave and (b) T-wave generated by photoacoustic phenomena [16].

2 Modeling of Generation and Propagation of PA Wave

2.1 The Governing Equations for Elastic Wave Propagation

The Cartesian coordinates (x_1, x_2, x_3) are used in this formulation. Since index notation is convenient for the expression in discretization, the summation convention rule is applied below. Let $\boldsymbol{x}$ and t be the position vector and time, respectively. We denote the stress and the strain in solid/fluid by $\sigma_{ij}(\boldsymbol{x}, t)$ and $\varepsilon_{ij}(\boldsymbol{x}, t)$, respectively. When the target

material is illuminated with a laser pulse with an energy less than the melting threshold of the material, a transient stress field is excited due to the thermoelastic expansion.

$$\sigma_{ij} = C_{ijkl}\varepsilon_{kl} - \beta_{ij}T \tag{1}$$

Above equation is known as the Duhamel-Neumann relation [12], which is used for the constitutive relation for a linear elastic body with a change in temperature $T(\boldsymbol{x}, t)$. Assuming the material is isotropic, the elastic stiffness tensor $C_{ijkl}(\boldsymbol{x})$ in Eq. (1) is expressed using the Lame constants $\lambda(\boldsymbol{x})$, $\mu(\boldsymbol{x})$ and Kronecker's delta tensor δ_{ij} as follows

$$C_{ijkl} = \lambda\delta_{ij}\delta_{kl} + \mu(\delta_{ik}\delta_{jl} + \delta_{il}\delta_{jk}) \tag{2}$$

In addition, $\beta_{ij}(\boldsymbol{x})$ in Eq. (1) can be written using the linear expansion coefficient $\alpha(\boldsymbol{x})$ for an isotropic material as in the following equation:

$$\beta_{ij} = (3\lambda + 2\mu)\alpha\delta_{ij} \tag{3}$$

Substituting Eqs. (2) and (3) into Eq. (1) and replacing the strain $\varepsilon_{ij}(\boldsymbol{x}, t)$ by the displacement $u_i(\boldsymbol{x}, t)$, we obtain

$$\sigma_{ij} = \lambda\frac{\partial u_k}{\partial x_k}\delta_{ij} + \mu\left(\frac{\partial u_i}{\partial x_j} + \frac{\partial u_j}{\partial x_i}\right) - (3\lambda + 2\mu)\alpha\delta_{ij}T \tag{4}$$

For the discretization of the FIT, we provide an expression for the time derivative of the above equation as

$$\dot{\sigma}_{ij} = \lambda\frac{\partial v_k}{\partial x_k}\delta_{ij} + \mu\left(\frac{\partial v_i}{\partial x_j} + \frac{\partial v_j}{\partial x_i}\right) - (3\lambda + 2\mu)\alpha\delta_{ij}\dot{T} \tag{5}$$

The dot $(\dot{\sigma}_{ij})$ on the character means the derivative in terms of time. The stress $\sigma_{ij}(\boldsymbol{x}, t)$ and velocity $v_i(\boldsymbol{x}, t)$ satisfy the following equation of motion

$$\rho\dot{v}_i = \frac{\partial\sigma_{ij}}{\partial x_j} \tag{6}$$

where $\rho(\boldsymbol{x})$ is the density.

In the FIT for wave propagation, we solve for the stress and velocity in Eqs. (5) and (6). In the case of PA waves, the time evolution of temperature must also be taken into account. The L-wave and T-wave velocities c_L and c_T in a solid, respectively, are expressed as follows

$$c_L = \sqrt{\frac{\lambda + 2\mu}{\rho}}, c_T = \sqrt{\frac{\mu}{\rho}} \tag{7}$$

To represent the acoustic wave in a fluid, $\mu(\boldsymbol{x}) = 0$ in Eq. (5). Also, since shear stress does not act in a fluid, $\sigma_{ij}(\boldsymbol{x}, t) = 0$ $(i \neq j)$ in Eq. (6).

2.2 The Governing Equations for Heat Conduction

When the laser is irradiating the material, the temperature $T(\boldsymbol{x}, t)$ is governed by the following heat conduction equation:

$$\rho c \dot{T} = -\frac{\partial q_i}{\partial x_i} + Q \tag{8}$$

where $c(\boldsymbol{x})$ is the specific heat at constant volume and $Q(\boldsymbol{x}, t)$ is the heat source. In Eq. (8), $q_i(\boldsymbol{x}, t)$ is the heat flux and satisfies the following Fourier's law

$$\frac{1}{k}q_i = -\frac{\partial T}{\partial x_i} \tag{9}$$

where $k(\boldsymbol{x})$ is the thermal conductivity.

To calculate the generation and propagation of PA waves due to laser irradiation, the velocity $v_i(\boldsymbol{x}, t)$, stress $\sigma_{ij}(\boldsymbol{x}, t)$, temperature $T(\boldsymbol{x}, t)$, and heat flux $q_i(\boldsymbol{x}, t)$ are solved using Eqs. (5), (6), (8), and (9). When the laser irradiates in the target area for a short time, the stress changes due to the rapid temperature rise, as shown in Eq. (5). Here, the deformation by the stress change has little effect on the temperature, so we solve a one-way coupled analysis in which the temperature change contributes to the deformation.

2.3 The Finite Integration Technique

Although the discretization for elastic wave equations was described in detail in past research [17], a coupled approach of the heat conduction and wave equations is focused on below. For simplicity, we consider a two-dimensional (2D) plane strain field (x_1, x_2). Integrating Eq. (5) over volume V and applying Gauss' divergence theorem, we obtain

$$\int_V \dot{\sigma}_{11}\mathrm{d}V = \int_S (\lambda + 2\mu)v_1 n_1 \mathrm{d}S + \int_S \lambda v_2 n_2 \mathrm{d}S - \int_V (3\lambda + 2\mu)\alpha \dot{T}\mathrm{d}V \tag{10}$$

where, $\boldsymbol{n}$ is the outward normal on V. As the integration volume V in Eq. (10), we consider a square cell with a side length of Δx. Assuming that stress and temperature are constant values in the integration cell, we obtain

$$\dot{\sigma}_{11}\Delta x^2 = (\lambda + 2\mu)\left[v_1^{(R)} - v_1^{(L)}\right]\Delta x + \lambda\left[v_2^{(U)} - v_2^{(D)}\right]\Delta x - (3\lambda + 2\mu)\alpha \dot{T}\Delta x^2 \tag{11}$$

where superscripts denote the positions of the physical quantities of the integral volume, as shown in Fig. 3(a). The material constants λ, μ, and ρ are assumed to be uniform in the integral cell of stress. Rewriting Eq. (11), we obtain the following equation.

$$\dot{\sigma}_{11} = \frac{(\lambda + 2\mu)}{\Delta x}\left[v_1^{(R)} - v_1^{(L)}\right] + \frac{\lambda}{\Delta x}\left[v_2^{(U)} - v_2^{(D)}\right] - (3\lambda + 2\mu)\alpha \dot{T} \tag{12}$$
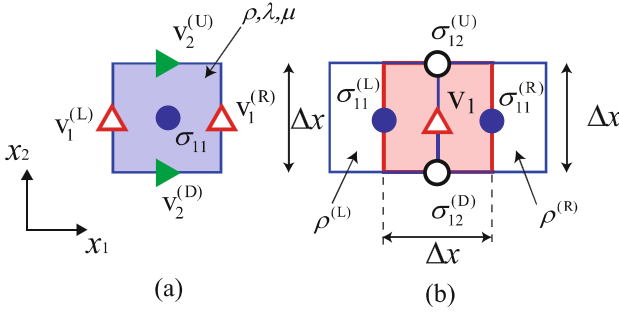
Fig. 3. Integration cells for (a) normal stress σ_{11} and (b) particle velocity v_1

Similarly, integrating and discretizing Eq. (6) yields

$$\dot{v}_1 = \frac{1}{\bar{\rho}_1 \Delta x}\Big[\sigma_{11}^{(R)} - \sigma_{11}^{(L)} + \sigma_{12}^{(U)} - \sigma_{12}^{(D)}\Big] \tag{13}$$

Since the density is given in the σ_{11} integration cell, as shown in Fig. 3(a), the average value $\bar{\rho} = \frac{1}{2}\big(\rho^{(L)} + \rho^{(R)}\big)$ is used in the integration of v_1, as shown in Fig. 3(b).

Next, we show the discretization of Eq. (8). Integrating Eq. (8) over volume V and applying Gauss' divergence theorem, we obtain

$$\int_V \rho c \dot{T} dV = -\int_S (q_1 n_1 + q_2 n_2) dS + \int_V Q dV \tag{14}$$

As shown in Fig. 4(a), the integration cell for T is denoted by blue color. From Eq. (5), it is convenient for the discretization to have a common grid for stress $\sigma_{ij}(\mathbf{x}, t)$ and temperature $T(\mathbf{x}, t)$. The parameters c, ρ, and k related to heat conduction are defined in the integral cell of T. Since T is assumed to be constant in the cell, Eq. (8) becomes.

$$\dot{T} = \frac{1}{\rho c \Delta x}\Big[q_1^{(L)} - q_1^{(R)} + q_2^{(D)} - q_2^{(U)}\Big] + \frac{Q}{\rho c} \tag{15}$$

Using Eq. (9), the discretization of q_1 is carried out in the same way. As shown in Fig. 4(b), k is defined by the integration cell for T, then we have

$$q_1 = \frac{\bar{k}_1}{\Delta x}\Big[T^{(L)} - T^{(R)}\Big] \tag{16}$$

where the averaging calculation is performed as $\bar{k}_1 = 2\Big/\Big(\frac{1}{k^{(L)}} + \frac{1}{k^{(R)}}\Big)$.
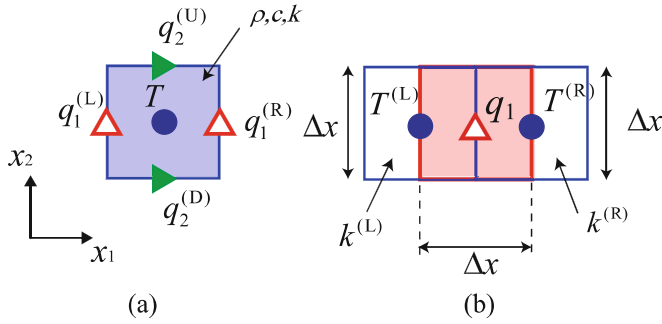
Fig. 4. Integration cells for (a) temperature T and (b) heat flux q_1

2.4 Coupled Analysis

The physical quantities are arranged on a grid, as shown in Fig. 5. Velocity and heat flux, normal stress, and temperature are placed on the same grid. The stresses and velocities are updated using the central difference approximation. In the time domain, the stress components σ_{ij} are allocated at half-time steps, while the velocities v_i are allocated at full-time steps. The following time discretization yields an explicit leap-frog scheme:

$$\{\sigma_{ij}\}^{z+1/2} = \{\sigma_{ij}\}^{z-1/2} + \Delta t \{\dot{\sigma}_{ij}\}^z \tag{17}$$

$$\{v_i\}^{z+1} = \{v_i\}^z + \Delta t \{\dot{v}_i\}^{z+1/2} \tag{18}$$

where Δt is the time step and the superscript z is the integer of the time step.

The temperature effect must also be considered in the calculation of $\dot{\sigma}_{ii}$ in Eq. (5). As shown in Eq. (17), the updates of the stresses are performed at the integer step z. Therefore, the temperature updates are computed in the integer step by using the forward-difference approximation as:

$$\{T\}^{z+1} = \{T\}^z + \Delta t \{\dot{T}\}^z \tag{19}$$

The entire calculation process is summarized below.

- Step 1: Determine the initial and boundary conditions [17].
- Step 2: Calculate heat transfer. Set the heat source Q and then calculate using Eq. (15). Also, update the temperature and heat flux using Eqs. (19) and (16), respectively.
- Step 3: Calculate the stresses. Using the data $\dot{T}^z$ obtained in Step 2, calculate the stress $\dot{\sigma}_{ij}^z$ in Eq. (12) and then obtain $\sigma_{ij}^{z+1/2}$ using Eq. (17).
- Step 4: Substitute $\sigma_{ij}^{z+1/2}$ into Eq. (13) to obtain $\dot{v}_i^{z+1}$. Then, substitute $\dot{v}_i^{z+1}$ into Eq. (18) to obtain the velocity field $v_i^{z+1/2}$.
- Step 5: Repeat Steps 2–4 for the estimated time step, and output the calculation results at the required interval.
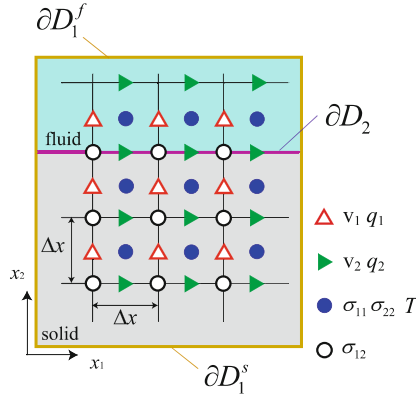
Fig. 5. Allocation of physical quantities in the 2D FIT

2.5 Stability Conditions for Coupled FIT

Since Eqs. (17)–(19) are explicitly updated, the numerical stability conditions must be fulfilled based on Von Neumann's stability analysis [18]. In the case of the 2D wave equation, the time step Δt must satisfy the following conditions:

$$\Delta t \leq \frac{1}{c_{L\max}} \frac{\Delta x}{\sqrt{2}} \tag{20}$$

where $c_{L\max}$ is the velocity of the fastest wave in the medium. To solve the 2D heat conduction equation with stability,

$$\Delta t \leq \frac{\rho c}{k} \frac{(\Delta x)^2}{4} \tag{21}$$

is required.

The laser pulse duration is short in the PA wave generation, so the time step Δt should be small. This means that the increment number becomes necessarily large, so the update with different time steps between Eqs. (17) and (19) is not beneficial from the standpoint of computational time. In this method, the solutions of the wave equation and the heat conduction equation are updated with the common Δt, which satisfies both Eqs. (20) and (21).

3 Numerical Simulation

3.1 Numerical Models

Figure 6(a) shows numerical model A when the laser is irradiated from air to aluminum. The simulation area (x_1, x_2) is a 5×4 mm rectangle with 0.1 mm absorption layers (perfectly matched layers) on the left, right and bottom sides of the region. Figure 6(b) shows numerical model B when the laser irradiation is from water. In model B, a water layer of 1 mm is placed on top of the aluminum. The material constants are listed in

Table 1. The cell size is set to $\Delta x = 0.5\ \mu m$, and the time step $\Delta t = 0.05$ ns. The center of the laser irradiation is $(x_1, x_2) = (2.5\ \text{mm}, 4.0\ \text{mm})$, and the spot radius of the laser and the pulse laser duration are defined as r_0 and t_0, respectively. The heat source Q is fed into the cell in the spot radius on the aluminum surface. In reality, the PA wave is generated in water by laser irradiation. However, the pressure of the PA wave generated on the aluminum surface is much greater than that in water because of the Grüneisen coefficient [11], representing the efficiency of light-to-heat conversion. In this study, therefore, we ignore the generation of PA waves in water.

Table 1. Material and thermal parameters for aluminum and water.

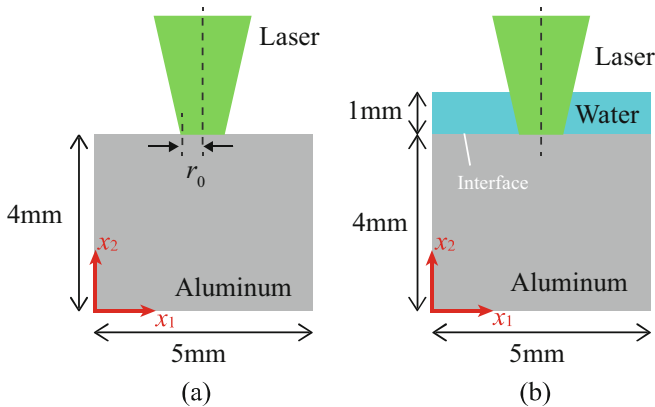| Material	Aluminum	Water
Density ρ (kg m^{-3})	2688	996.6
Longitudinal wave velocity c_L (m s^{-1})	6400	1470
Transverse wave velocity c_T (m s^{-1})	3150	–
Linear expansion coefficient α (K^{-1})	2.31×10^{-5}	1.00×10^{-4}
Specific heat c (J kg^{-1} K^{-1})	905	4179
Thermal conductivity k (W m^{-1} K^{-1})	237	0.6104

Fig. 6. (a) Numerical model of laser irradiation from air to aluminum body (Model A), (b) numerical model of laser irradiation from water to aluminum body (Model B)

3.2 Simulation Result for Model A

Figure 7 shows the simulation results in Model A when the laser pulse duration t_0 is 7 ns, and the spot radius r_0 is 0.05 mm. The plots of the Mises stress at $t = 320$ and 480 ns after laser irradiation are shown in Fig. 7. The stress values are normalized by dividing the maximum value throughout the entire time step. First, it is shown that the L-wave is

generated mainly in the direction of 60°, not in the x_2 axis direction. On the other hand, the T-wave has more significant stress in the direction of 30° than the L-wave. It can be seen that the wave propagation directions in Fig. 7 are in good agreement with the directivity pattern, as shown in Fig. 2.

Figure 8 shows the simulation results when the spot radius r_0 is 0.428 mm. Here we consider two types of laser pulse duration t_0. One is 7 ns, and the other is 30 ns. In Fig. 8(a), an L-wave wavefront with a small amplitude can be seen in the x_2 axis direction. The generation of this L-wave wave is caused by the finite spot radius. On the other hand, the Rayleigh waves in the x_1 direction are smaller than those in Fig. 7. Figure 8(b) shows the simulation results in the case of the laser pulse duration $t_0 = 30$ ns while keeping the spot radius $r_0 = 0.428$ mm. The L-wave is hardly seen in the x_2 axis direction. The amplitude of T-waves becomes smaller than in Fig. 8(a).

Let us summarize these simulation results. The key point to increase the gain of the PA wave is that light-thermal conversion takes place in a brief period. Also, the directivity pattern of the PA wave shown in Fig. 2 is applicable when the pulse duration is short, and the spot area is small. Nevertheless, it was demonstrated that the L-wave could be generated in the bottom direction if the laser spot area gets to a specific size.
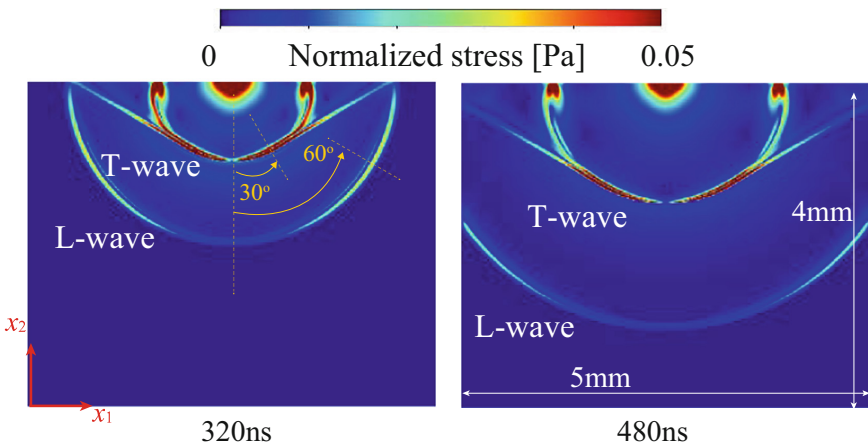

Fig. 7. Snapshots of PA wave generated by laser irradiation in the case of the laser pulse duration $t_0 = 7$ ns and spot radius $r_0 = 0.05$ mm in Model A.

3.3 Simulation Result for Model B

Figure 10 shows the simulation results for Model B when the laser pulse duration t_0 is 7 ns, and the spot radius r_0 is 0.428 mm. It can be seen that pressure (P) waves in water as well as the L- and T-waves in aluminum are generated. The amplitude of the L-wave generated in the x_2 axis direction in aluminum is more significant than that of the laser irradiation in the air. This is considered because the presence of water at the top layer exerts a reaction force on the vertical stress in the solid against the thermal expansion, and then the amplitude of the PA wave in the x_2 axis direction becomes large.
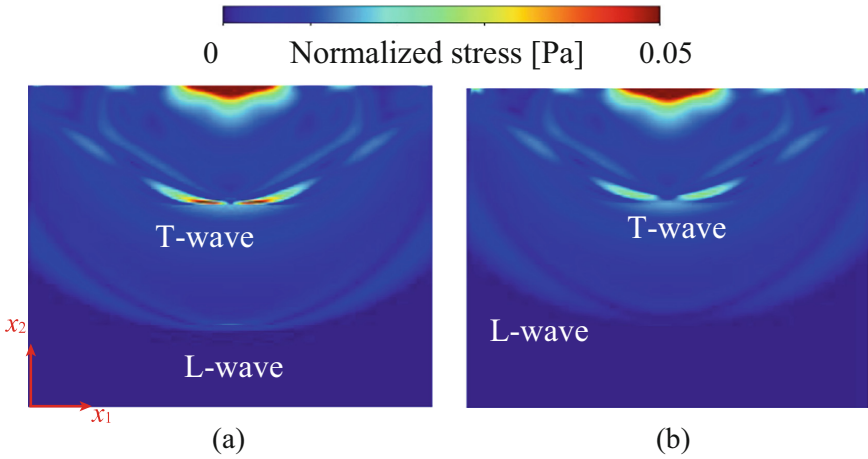
Fig. 8. Snapshots of the PA wave at $t = 480$ ns in the case of the spot radius $r_0 = 0.428$ mm in Model A. (a) Laser pulse duration $t_0 = 7$ ns and (b) $t_0 = 30$ ns.

In the next section, this phenomenon is validated by experimental measurement of the PA wave (Fig. 9).
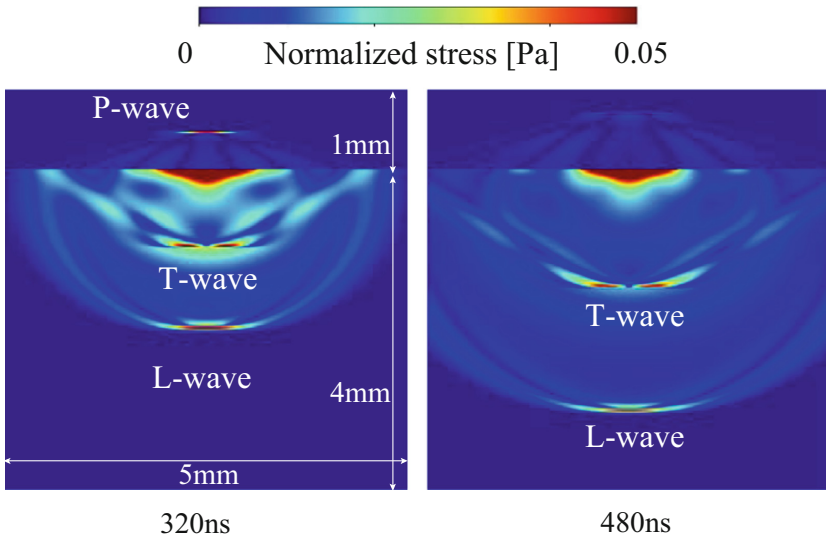

Fig. 9. Snapshots of PA wave generated by laser irradiation in water (Model B). The laser pulse duration $t_0 = 7$ ns and spot radius $r_0 = 0.428$ mm.

4 Validation by PA Wave Measurement

In this experiment, the laser irradiation is scanned, and the generated PA waves are received by a fixed ultrasonic probe. Although the frequency range of the PA wave is wide in reality, the PA waves are modulated by the bandwidth of the receiving probe. Therefore, this experiment cannot be directly compared with the previous section's simulation. Still, the generation of L- and T-waves and their spreading are helpful to validate the simulation.

4.1 Experimental Setup and Specimen

Figure 10 shows the system configuration for acquiring photoacoustic waves. The generation of laser light is driven by a compact Q-switched Nd:YAG laser operating at approximately 1.0 mJ pulse energy (Nano L90-100, Litron). The laser light source emits a laser with a wavelength of 532 nm and a pulse duration of 7.0 ns. The generated PA waves are detected using an ultrasonic probe (V112-RM, Olympus) with a radius of approximately 6.4 mm and a center frequency of 10 MHz. The measured signals are digitized at a sampling rate of 100 MS/s. Figure 11 shows the laser scan area on an aluminum specimen ($c_L = 6400$ m/s and $c_T = 3150$ m/s). The size of both specimens is $100 \times 100 \times 10$ mm. Figures 11(a) and (b) show the cases of laser irradiation from the air and water, respectively. The laser spot radius is approximately 0.43 mm. We scan for 60 mm in the x direction at a pitch of 0.05 mm while recording the waveform at the probe for each irradiation.
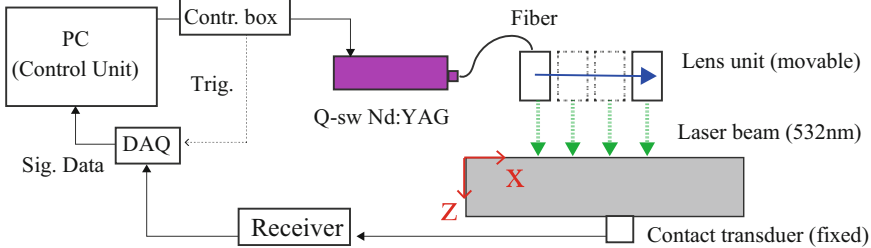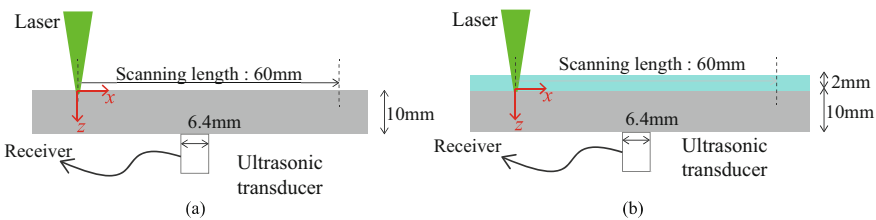

Fig. 10. Flaw diagram of PA measurement system.

Fig. 11. Experiment in the case of laser irradiation from (a) air and (b) water

4.2 Experimental Results

In Fig. 12, time history waveforms at each irradiation in the *x*-direction are plotted throughout the scan. The vertical and horizontal axes are the arrival time of the signal and scanning point, respectively. The L-wave arrives at approx. 1.6 μs, and the T-wave arrives later in Fig. 12. From Fig. 12(a), we can observe the L-wave propagating in the bottom direction of the specimen. The L-wave propagates in the vertical direction at the simulation result in Fig. 8(a), and the measurement shows similar results to the simulation. Figure 12(b) shows the measurement results when a laser is irradiated onto aluminum from water. The amplitude of the L wave is larger than the measurement result in the case of laser irradiation from the air. As the simulation results are shown in Fig. 9, we can observe the amplitude of the L-wave propagating in the vertical direction becomes more significant in water in Fig. 12(b). The above measurement results show the same tendency concerning the L- and T-waves generation as the simulation models A and B.
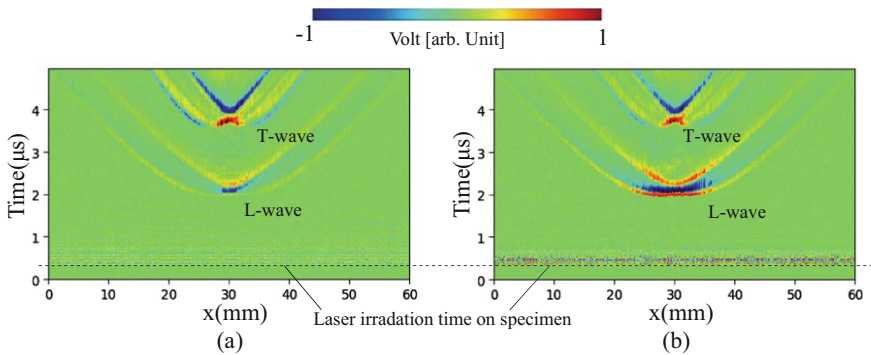

Fig. 12. Time history waveforms at each irradiation in the *x*-directional scan. The vertical and horizontal axes are the arrival time of the signal and scanning point, respectively. The color shows the amplitude of waveforms in the case of laser irradiation from (a) air and (b) water.

5 Concluding Remarks

In this study, simulations were presented to simulate the PA wave generation and propagation in solid and water. To model the phenomena, we numerically solved the coupled heat conduction equation and wave equation using the FIT. It was shown that the PA waves generated by laser irradiation varied depending on the spot size, laser pulse duration, the material surface condition, and others. We simulated two cases where the laser was irradiated on the target material in the air and underwater. The amplitude of the L-wave propagating in the bottom direction in the case of laser irradiation in water becomes more extensive than in the case of laser irradiation in the air. This reason was assumed that the presence of water in the upper part generated a reaction force against the stress caused by thermal expansion. A similar trend was observed in the measurement; therefore, the proposed FIT modeling was well-validated by the experiment.

We did not reach a direct comparison between the simulation and the experiment in this study. The comparison requires a measurement device such as a laser Doppler vibrometer, which can receive the PA signal at a narrow area. In the future, we would like to extend the 2D simulation to large-scale 3D calculation and model the generation of ultrasonic waves by ablation.

References

1. Wakata, S., Hosoya, N., Hasegawa, N., and Nishikino, M.: Defect detection of concrete in infrastructure based on Rayleigh wave propagation generated by laser-induced plasma shock waves, Int. J. Mech. Sci. 218, 107039 (2022).
2. Shimada, Y., Kotyaev, O., Kurahashi, S., Yasuda, N., Misaki, N., Takayama, Y., and Soga, T.: Development of laser-based remote sensing technique for detecting defects of concrete lining, Electron. Comm. Jpn. 102, 12–18 (2019).
3. Monchalin, J.P.: Laser-ultrasonics: principles and industrial application, Proceedings in Ultrasonic and Advanced Methods for Nondestructive Testing and Material Characterization, 79–115 (2007).
4. Nomura, K., Deno, S., Matsuida, T., Otaki, S., and Asai, S.: In situ measurement of ultrasonic behavior during lap spot welding with laser ultrasonic method, NDT & E Int. 130, 102662 (2022).
5. An, Y.K., Park, B., and Sohn, H.: Complete noncontact laser ultrasonic imaging for automated crack visualization in a plate, Smart Mater. Struct. 22(2), 025022 (2013).
6. Choi, S. and Jhang, K.Y.: Internal defect detection using laser-generated longitudinal waves in ablation regime, J. Mech. Sci. Technol. 32, 4191–4200 (2018).
7. Scherr, J.F., Kollofrath, J., Popovics, J.S., Bühling, B., and Grosse, C.U.: Detection of delaminations in concrete plates using a laser ablation impact echo technique, J. Nondestruct. Eval. 42, 11 (2023).
8. Wang, L., and Hu, S.: Photoacoustic tomography: in vivo imaging from organelles to organs, Science 335, 1458–1462 (2012).
9. Zhang, H.F, Maslov, K., Stoica, G., and Wang, L.V.: Functional photoacoustic microscopy for high-resolution and noninvasive in vivo imaging, Nat. Biotechnol. 24(7), 848–851 (2006).
10. Saijo, Y., Ida, T., Iwazaki, H., Miyajima, J., Tang, H., Shintate, R., Sato, K., Hiratsuka, T., Yoshizawa, S., and Umemura, S.: Proceedings in Photons Plus Ultrasound: Imaging and Sensing 2019, 108783E (2019).
11. Okawa, S., Hirasawa, T., Kushibiki, T., and Ishihara, M.: Numerical evaluation of linearized image reconstruction based on finite element method for biomedical photoacoustic imaging, Opt. Rev. 20, 442–451 (2013).
12. Scruby, C. B., Dewhurst, R. J., Hutchins, D. A., and Palmer, S. B.: Quantitative studies of thermally-generated elastic waves in laser-irradiated metals, J. Appl. Phys. 51, 6210–6216 (1980).
13. Yoshikawa, H., Ohta, Y., and Nishimura, N.: Crack determination using laser-measured horizontal and vertical velocity waveforms of ultrasound, Struct. Eng. / Earthquake Eng. 23(2), 279–285 (2006).
14. Soltani, P. and Akbareian, N.: Finite element simulation of laser generated ultrasound waves in aluminum plates, Lat. Am. J. Solids. Struct. 11, 1761–1776 (2014).

15. Zhu, Z., Sui, H., Yu, L., Zhu, H., Zhang, J., and Peng, J.: Effective defect features extraction for laser ultrasonic signal processing by using time-frequency analysis, in IEEE Access 7, 128706–128713 (2019).
16. Scruby, C. B.: Some applications of laser ultrasound, Ultrasonics 27(4), 195–209 (1989).
17. Fellinger, P., Marklein, R., Langenberg, K.J., and Klaholz, S.: Numerical modeling of elastic wave propagation and scattering with EFIT - elastodynamic finite integration technique, Wave Motion 21(1), 47–66 (1995).
18. Isaacson, E. and Keller, B. H.: Analysis of Numerical Methods, Courier Corporation, 1994.